







RESEARCH ARTICLE | OCTOBER 12 2023

## Numerical analysis of the effect of an oscillating metal vapor plume on the keyhole and molten pool behavior during deep penetration laser beam welding

Special Collection: [Proceedings of the International Congress of Applications of Lasers & Electro-Optics \(ICALEO 2023\)](#)

Fan Yang ; Xiangmeng Meng ; Stephen Nugraha Putra ; Antoni Artinov ; Marcel Bachmann ; Michael Rethmeier 



*J. Laser Appl.* 35, 042041 (2023)

<https://doi.org/10.2351/7.0001094>



CrossMark



Journal of  
Laser Applications

[Learn More](#)



RAPID TIME  
TO ACCEPTANCE



COMMUNITY  
DRIVEN



EXPANSIVE  
COVERAGE



PRESTIGIOUS  
EDITORIAL BOARD



EXTENSIVE  
MARKETING

# Numerical analysis of the effect of an oscillating metal vapor plume on the keyhole and molten pool behavior during deep penetration laser beam welding

Cite as: J. Laser Appl. 35, 042041 (2023); doi: 10.2351/7.0001094

Submitted: 24 June 2023 · Accepted: 13 September 2023 ·

Published Online: 12 October 2023



View Online



Export Citation



CrossMark

Fan Yang,<sup>1</sup> Xiangmeng Meng,<sup>1</sup> Stephen Nugraha Putra,<sup>1</sup> Antoni Artinov,<sup>1</sup> Marcel Bachmann,<sup>1</sup>   
and Michael Rethmeier<sup>1,2,3</sup>

## AFFILIATIONS

<sup>1</sup>Bundesanstalt für Materialforschung und -prüfung (BAM), Unter den Eichen 87, Berlin 12205, Germany

<sup>2</sup>Institute of Machine Tools and Factory Management, Technische Universität Berlin, Pascalstraße 8-9, Berlin 10587, Germany

<sup>3</sup>Fraunhofer Institute for Production Systems and Design Technology, Pascalstraße 8-9, Berlin 10587, Germany

**Note:** Paper published as part of the special topic on Proceedings of the International Congress of Applications of Lasers & Electro-Optics 2023.

## ABSTRACT

The effect of the oscillating metal vapor plume on the keyhole and molten pool behavior during the laser beam welding of AlMg3 aluminum alloys is investigated by experimental and numerical methods. The real-time height of the metal vapor plume is measured by high-speed camera observation. The obtained experimental results are used to evaluate the additional heating source and laser beam attenuation caused by the scattering and absorption based on the Beer–Lambert theory. Furthermore, the dynamic behavior of the metal vapor plume is incorporated into a 3D transient heat transfer and fluid flow model, coupled with the ray tracing method, for the laser beam welding of the AlMg3 alloy. It is found that additional heating resulting from the scattered and absorbed laser beam energy by the metal vapor plume significantly expands the shape of the molten pool on the top region. Moreover, the oscillating metal vapor plume caused the fluctuation of the high-temperature region in the molten pool. The probability of keyhole collapse at the bottom increases 17% due to the oscillating laser power induced by the laser beam attenuation. The internal interplay between the metal vapor plume, molten pool shape, and keyhole collapse is obtained. The developed model has been validated by experiments, which shows a good agreement.

Key words: deep penetration laser beam welding, numerical simulation, oscillating vapor plume, keyhole collapse

© 2023 Author(s). All article content, except where otherwise noted, is licensed under a Creative Commons Attribution (CC BY) license (<http://creativecommons.org/licenses/by/4.0/>). <https://doi.org/10.2351/7.0001094>

## I. INTRODUCTION

Deep penetration laser beam welding (LBW) has emerged as a promising technology with applications in the aerospace, large high-pressure and vacuum vessel industries, and shipbuilding, owing to the rapid advancements in high-power laser sources (>10 kW, up to 100 kW).<sup>1</sup> One of the distinguished features of deep penetration LBW is the formation of a keyhole, which is a narrow and deep cavity. This keyhole is formed when the intense energy from the laser beam vaporizes a part of the liquid metal, leading to the

downward recoil pressure.<sup>2</sup> Once the metal vapor is ejected from the keyhole, it can be condensed to metal nanoparticles, which significantly influences the laser radiation. The keyhole, weld pool, and the metal vapor plume are self-consistently interconnected throughout the deep penetration LBW process. Their coupled behavior is closely associated with the generation of welding defects, such as spatter and process porosity. Consequently, the intricate relationships among the keyhole, weld pool, and metal vapor plume have gained increasing attention over the past decades.

The influence of the metal vapor plume on the behavior of the molten pool and keyhole is comprehensive and multiplicate. Compared to LBW with the application of CO<sub>2</sub> laser, the laser beam attenuation caused by the inverse bremsstrahlung absorption is lower, and the metal vapor plume is weakly ionized during fiber LBW due to the lower inverse bremsstrahlung absorption coefficient.<sup>3</sup> However, the nanoparticle nucleation process is initiated by the rapid cooling of the vapor plume ejected from the keyhole.<sup>4</sup> The presence of these particles in the metal vapor plume leads to the attenuation of the laser beam through scattering and absorption before reaching back to the base metal surface. Scattering refers to the phenomenon where the waves, light, or sound change their propagation path while passing through a medium. When the laser beam collides with the nanoparticles in the metal vapor plume, scattering and energy absorption happen among these nanoparticles. It is important to note that a part of the laser beam energy can be transferred back to the molten pool in different ways.

The nanoparticles existing in the plume have a significant impact on the keyhole and molten pool behavior and thus influence the welding quality. The attenuation was calculated by Shcheglov *et al.* when the fiber laser beam propagates through the metal vapor plume. Their findings revealed an attenuation value of up to 12%, which can lead to instability of the welding process.<sup>5</sup> Zou *et al.* clarified the effect of the laser-induced metal vapor plume with different heights on weld penetration during high-power fiber LBW. It was found that the weld penetration could increase by 20% as the metal vapor plume was blown away by using the supersonic cross jet. This can be attributed to the elimination of laser beam attenuation caused by the particles in the metal vapor plume.<sup>6</sup> Reijonen *et al.* studied the effect of shielding gas flow velocity on the porosity ratio in fiber laser powder bed fusion additive manufacturing. They concluded that the porosity ratio was increased due to the attenuation effect produced by the metal vapor plume when the insufficient cross-flow of shielding gas was employed.<sup>7</sup> Although the substantial influence of the metal vapor plume on the dynamic keyhole and molten pool, as well as its consequential effect on the welding quality has gained increasing recognition, the essential characteristic of the oscillating ejection has not been investigated in detail. The oscillating ejection of the metal vapor plume results in the oscillating laser beam attenuation due to the scattering and absorption effects. It is a challenge to quantitatively describe the influence of the oscillating laser beam attenuation on the dynamic keyhole and molten pool by experimental methods.

An insight into the complicated interactional mechanism between the keyhole, molten pool, and metal vapor plume can be obtained by using a sophisticated numerical simulation model. The vapor jet during the LBW of steel is calculated by a fully triple-phase coupled solid-liquid-gas model published by Pang *et al.*<sup>8</sup> In their model, the thermal effect, momentum effect, as well as the coupling effect caused by the metal vapor plume were considered. Different from the aforementioned time-consuming full triple-phase coupled model, Cho *et al.* proposed a more accessible analytical method, including the momentum and thermal effects of the metal vapor plume.<sup>9</sup> However, the above research did not consider the laser beam attenuation caused by the scattering and absorption effect due to the condensed metal nanoparticles. Based on the triple-phase coupled model and sharp interface formulation, Tan

*et al.* studied the effect of vapor plume attenuation on the keyhole and molten pool behavior during LBW of steel.<sup>10,11</sup> According to their studies, the interplay of the multiple reflections and plume attenuation is crucial for the laser absorption intensity on the keyhole wall. Hence, the fluid flow in the molten pool is also influenced profoundly. Han *et al.* recently reported that the scattering effect by the nanoparticles in the metal vapor plume is considered by calculating the actual scattering route based on the Rayleigh scattering model. Meanwhile, the absorption effect was also included in their work by reducing the energy of the subray in the ray tracing algorithm.<sup>12</sup>

According to the above literature review, although the significance of the interconnection between metal vapor plume, keyhole, and molten pool behavior has been recognized, the influences of oscillating metal vapor plume on the keyhole and molten pool behavior have not been studied systematically. Previous studies mainly focused on the metal vapor plume effects in the LBW of steel, while the LBW of aluminum presents unique characteristics and challenges, particularly regarding the influence of the metal vapor plume on the keyhole and molten pool. This paper has developed a 3D transient multiphysical numerical model including the oscillating laser beam attenuation caused by the scattering and absorption effect due to the nanoparticles in the metal vapor plume based on the experimental results and our previous work. The influence of the metal vapor plume on the keyhole and molten pool behavior has been revealed through the comparison between cases with/without the consideration of the metal vapor plume.

## II. EXPERIMENTAL SETUP

The experimental setup for capturing the metal vapor plume by a high-speed camera is shown in Fig. 1. Experiments on bead-on-plate welding were conducted using an IPG YLR 20000 LBW system. The welding parameters employed are provided in Table I. The base metal used is 5754 aluminum alloy, with dimensions of 300 × 100 × 10 mm<sup>3</sup>. The laser beam is inclined forward at

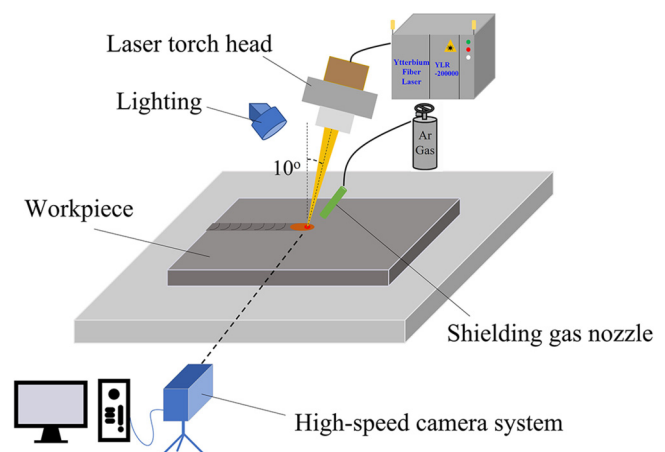


FIG. 1. Experimental setup for capturing metal vapor plume using high-speed camera.

10 November 2023 09:37:13

TABLE I. Laser beam welding parameters.

Parameters	Value
Laser power	5 kW
Laser spot diameter at the focal plane	0.52 mm
Wavelength	1070 nm
Focal position	0 mm
Welding speed	2 m/min

an angle of 10°. Pure Ar is used as shielding gas with a flow rate of 20 l/min (11.79 m/s at the nozzle outlet). A high-speed camera (Photron FASTCAM SA4) is used to capture the temporal evolution of the metal vapor plume ejected from the keyhole at a frequency of 10 000 Hz. The camera is positioned on the side at the same height as the plate and without any tilt angle.

### III. MATHEMATICAL MODELING

A three-dimensional transient multiphysical model, including the oscillating metal vapor plume, has been developed coupled with the volume of fluid (VOF) method to calculate the heat transfer, fluid flow, and keyhole dynamics. Due to the highly complex and coupled nature of the metal vapor plume, keyhole, and fluid flow behavior, certain simplifications have been applied to reduce computational costs. The assumptions made in the model are as follows:

- The flow regime of the liquid metal flow is assumed to be laminar, with the liquid metal being treated as Newtonian and incompressible. The buoyance term follows the Boussinesq approximation.
- The influence of shielding gas on the metal vapor plume has been indirectly included during the measurement of the vapor plume length in the experimental part, while the momentum effect from the shielding gas has been neglected in this model after the evaluation of the stagnation pressure on the plate induced by the shielding gas.
- The energy scattered and absorbed by the metal vapor plume is assumed to be fully transferred back into the melt pool.

#### A. Governing equation

The governing equations in a fixed Cartesian coordinates system can be mathematically expressed as follows:

##### 1. Mass equation

$$\nabla \cdot \vec{v} = 0, \quad (1)$$

where  $\vec{v} = (v_x, v_y, v_z)$  is the fluid velocity vector.

##### 2. Momentum equation

$$\rho \left( \frac{\partial \vec{v}}{\partial t} + (\vec{v} \cdot \nabla) \vec{v} \right) = -\nabla p + \mu \nabla^2 \vec{v} + \rho \vec{g} - \beta \rho (T - T_{Liq}) \vec{g} - \mu K \vec{v} + \vec{S}_m, \quad (2)$$

where  $\rho$  is the material density,  $t$  is the time,  $p$  is the pressure,  $\mu$  is the viscosity,  $\vec{g}$  is the vector of the gravity acceleration,  $T$  is the temperature,  $T_{Liq}$  is the liquidus temperature, and  $K$  is the Carman-Kozeny coefficient.<sup>13</sup>  $\vec{S}_m$  is the additional momentum source, which includes the effects of surface tension along the aluminum-air interface, the recoil pressure induced by evaporation, and the stagnation pressure and shear stress produced by the metal vapor plume. Due to the utilization of the VOF method, the continuum surface force method is employed to convert all surface forces into volumetric forces.<sup>14</sup>

### 3. Energy equation

$$\rho \left[ \frac{\partial h}{\partial t} + (\vec{v} \cdot \nabla) h \right] = \nabla \cdot (k \nabla T) + S_q, \quad (3)$$

where  $h$  is the enthalpy,  $k$  is the thermal conductivity, and  $S_q$  is the energy source term, which includes the laser heat flux density, convective and radiative heat transfer, evaporation, recondensation, as well as the energy resulted from the scattering and absorption effect by the metal vapor plume. It is noteworthy that the heat fluxes with the unit of W/m<sup>2</sup> described above should be converted to power densities with W/m<sup>3</sup>.<sup>15</sup>

### 4. VOF equation

$$\frac{\partial \phi}{\partial t} + \nabla \cdot (\vec{v} \phi) = 0, \quad (4)$$

where  $\phi$  is the volume fraction of aluminum.<sup>16</sup> The VOF equation is employed to track the transient deformation of the free surface including the keyhole surface, molten pool surface, and the solidified weld seam profile.

## B. Physical models included in LBW

### 1. Heat source model

The energy density distribution of the laser beam profile on an arbitrary horizontal plane is assumed to be an ideal Gaussian distribution, which can be mathematically expressed as follows:

$$q_L = \frac{2P_L}{\pi r_z^2} \cdot \exp\left(-2 \frac{x^2 + y^2}{r_z^2}\right), \quad (5)$$

$$r_z = r_f \left[ 1 + \left( \frac{z - z_f}{z_r} \right)^2 \right]^{\frac{1}{2}}, \quad (6)$$

where  $q_L$  is the heat density function,  $P_L$  is the laser power,  $r_z$  is the radius of the laser beam at  $z$  distance away from the focal plane,  $r_f$  is the laser beam radius at the focal plane,  $z_f$  is the position of the focal plane, and  $x$  and  $y$  are the coordinates.

A ray tracing algorithm is employed to calculate the ray reflections, which discretizes the laser beam energy into multiple energy bundles.<sup>17</sup> To improve the precision of the ray tracing algorithm, a potential cell on the reflection point is further divided into finer

virtual cells from 0.2 to 0.067 mm without burdening the calculation costs as the virtual refined ray tracing method is applied.<sup>18,19</sup> The Fresnel absorption happening on every reflection can be calculated by the following equation:

$$\alpha = 1 - \frac{1}{2} \left( \frac{1 + (1 - \varepsilon \cos \varphi)^2}{1 + (1 + \varepsilon \cos \varphi)^2} + \frac{\varepsilon^2 - 2\varepsilon \cos \varphi + 2 \cos^2 \varphi}{\varepsilon^2 + 2\varepsilon \cos \varphi + 2 \cos^2 \varphi} \right), \quad (7)$$

where  $\varphi$  is the angle between the incident ray and the surface normal,  $\varepsilon$  is a coefficient determined by the laser type and the material properties, which is set to 0.12 in this model.

### 2. Recoil pressure model

The improved recoil pressure model with the consideration of ambient pressure is used here,<sup>20</sup> and the recoil pressure can be calculated as

$$P_{recoil} = \begin{cases} 0, & 0 \leq T \leq T_L, \\ aT^3 + bT^2 + cT + d, & T_L \leq T \leq T_H, \\ 0.54P_0 \exp\left(\Delta L_v M \frac{T - T_b}{RTT_b}\right) - P_0, & T_H \leq T, \end{cases} \quad (8)$$

where  $T$  is the temperature;  $T_L$  is the low vaporization threshold ( $T_L = 2550$  K);  $T_H$  is the high vaporization threshold ( $T_H = 3600$  K);  $a$ ,  $b$ ,  $c$ , and  $d$  are the coefficient to guarantee a smooth transition in the vaporization temperature range ( $a = 1.38779773 \times 10^{-3}$ ,  $b = -1.12888349 \times 10^{-3}$ ,  $c = 3.07874688 \times 10^4$ , and  $d = -28113899.9$ );  $P_0$  is the atmospheric pressure;  $\Delta L_v$  is the latent heat of vaporization;  $M$  is the molar mass;  $R$  is the gas constant; and  $T_b$  is the boiling temperature. Since the ambient pressure can be considered a reference pressure or operating pressure, there is no necessity to apply it in the model. Instead, the recoil pressure below  $T_L$  can be applied as zero.

### 3. Capillary pressure and Marangoni stress

The temperature-dependent surface tension induces two distinct components: capillary pressure acted on the normal direction to the free surface and Marangoni stress exerted in the tangential direction. The normal capillary pressure  $\vec{P}_{ca}$  serves as the primary driving force for balancing the recoil pressure, significantly impacting the keyhole geometry. Simultaneously, the tangential Marangoni shear stress  $\vec{\tau}_{ma}$  plays a crucial role in influencing the fluid flow pattern. The normal capillary pressure  $\vec{P}_{ca}$  and the tangential Marangoni stress  $\vec{\tau}_{ma}$  can be written as follows:

$$\vec{P}_{ca} = \gamma \kappa \vec{n}, \quad (9)$$

$$\vec{\tau}_{ma} = \frac{\partial \gamma}{\partial T} \frac{\partial T}{\partial \vec{s}}, \quad (10)$$

where  $\gamma$  is the surface tension of aluminum,<sup>21</sup>  $\kappa$  is the curvature,  $\vec{n}$  is the normal unit vector, and  $\vec{s}$  is the tangential vector of the keyhole surface.

### 4. Recondensation model

The effective estimation of vapor recondensation flux within the inner region of the keyhole during the evaporation process has

been published.<sup>22</sup> The recondensation heat flux is determined by allocating 18% of the heat loss from evaporation as local recondensation, while the remaining 72% is assumed to be redistributed as surface heat flux along the keyhole. The rest of the energy is dissipated. This redistribution of recondensation heat linearly changes from zero at the keyhole bottom to its maximum value at the keyhole exit.

### 5. Metal vapor plume model

As mentioned in the Introduction, the laser beam can be attenuated by the scattering and absorption effects from the metal nanoparticles in the metal vapor plume. Based on our previous work, the amount of the attenuated laser beam energy by scattering and absorption can be calculated by Beer's law, as shown in the following equations:

$$\Delta I = I_0 [2 - \exp(-\alpha_{scattering} L) - \exp(-\alpha_{absorption} L)], \quad (11)$$

$$\alpha_{scattering} = \frac{2\pi^5 D_p^6 N}{3\lambda^4} \left| \frac{\eta^2 - 1}{\eta^2 + 2} \right|^2, \quad (12)$$

$$\alpha_{absorption} = \frac{\pi^2 D_p^3 N}{\lambda} \text{Im} \left( \frac{\eta^2 - 1}{\eta^2 + 2} \right), \quad (13)$$

where  $\alpha_{scattering}$  is the scattering coefficient and  $\alpha_{absorption}$  is the absorption coefficient,  $D_p$  is the particle diameter in the metal vapor plume ( $D_p = 110$  nm),  $N$  is the particle density ( $N = 1.2 \times 10^{16} \text{ m}^{-3}$ ),  $\lambda$  is the laser wavelength, and  $\eta$  is the complex refractive index of the nanoparticles in the metal vapor plume ( $\eta = 1.37 + 10.31i$ ), and  $L$  is the effective length of the metal vapor plume along the path of the laser propagation. The periodic effective length is fitted from the experimental measurements, as shown in Fig. 2.

Figure 2 shows the captured images of the metal vapor plume, its effective length, and the fitted results. As shown in Fig. 2(a), the ejected metal vapor plume can be blown away from the laser propagation path by the shielding gas, and thereby it may not be continuous. Meanwhile, multiple metal vapor plumes blocking the laser radiation simultaneously is an occasional situation during the welding process. Therefore, the effective length for the scattering and absorption effects is defined as the total length of the metal vapor plume along the path of the laser propagation. The effective length of the metal vapor plume was measured within a 200 ms timeframe, as illustrated in Fig. 2(b). Based on the statistical analysis, the metal vapor plume demonstrates periodic oscillations with the welding time. It is nonrepresentative to input the original experimental data within 200 ms into the numerical model. It is feasible and accessible to use a function to describe the oscillating height of a vapor plume. Therefore, the fast Fourier transform (FFT) algorithm was employed to identify the primary frequency characteristic of metal vapor ejection, which was determined to be 125 Hz. The peak height of the ejected metal vapor plume is defined as 9 mm, which is a mean value above a threshold. Since the vapor plume does not exist continuously, the duty cycle is determined as 0.67 based on the experimental data. The sine

10 November 2023 09:37:13

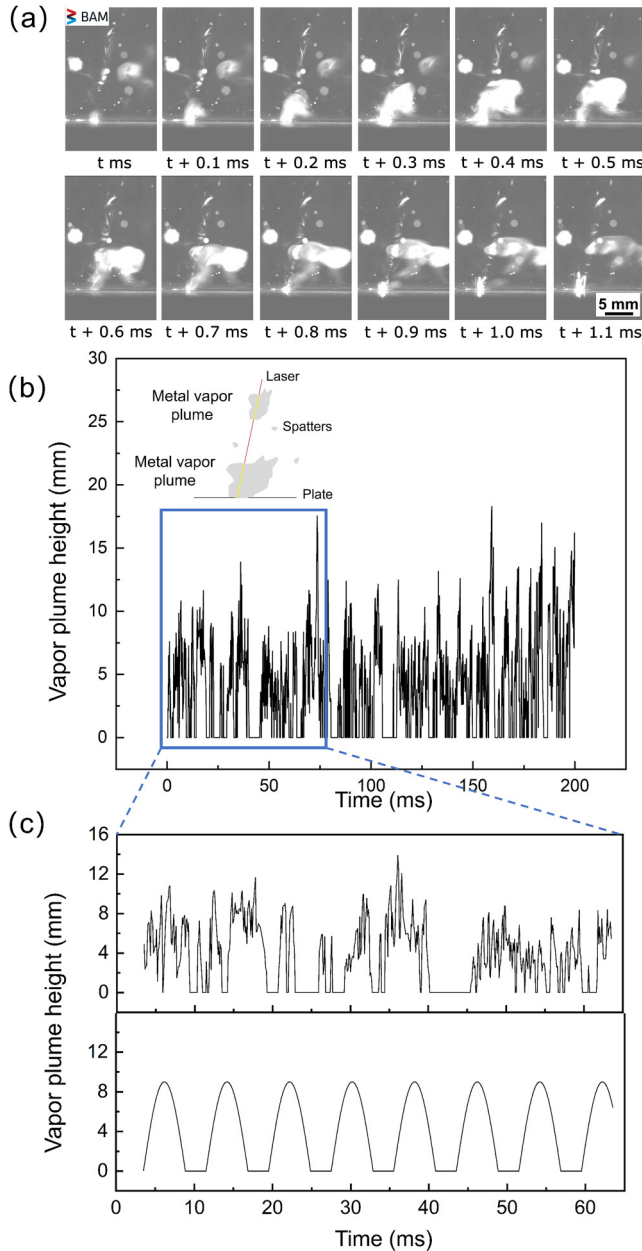


**FIG. 2.** The captured images of the metal vapor plume and its statistical results: (a) pictures of the generation and dissipation process of the metal vapor plume; (b) experimental results of the effective length of the metal vapor plume; (c) fitted results of the effective length by a sine function.

function is applied to fit the vapor plume height with the welding time, the fitted result is shown in Fig. 2(c). This fitted sine function is incorporated into Eq. (11) to account for the influence of the oscillating metal vapor plume. According to Eq. (11), when the vapor plume height reaches the maximum value of 9 mm, the

power ratio affected by the scattering effect is 3.01%, and the ratio affected by absorption is 0.99%.

The scattering effect results in the laser propagation route deviating from the original routes. Most of the deviated laser rays can reach the top surface of the metal plate. Therefore, the energy distribution on the top surface caused by the scattering effect is assumed to be a Gaussian distribution, as expressed in the following:

$$q_{\text{scattering}} = \frac{3 \cdot \alpha_{\text{scattering}} \cdot P_L}{\pi r_v^2} \cdot \exp\left(-3 \frac{x^2 + y^2}{r_v^2}\right), \quad (14)$$

where  $r_v$  is the effective radius of the Gaussian distribution. Here, the effective radius of the Gaussian distribution is defined as 1 mm.<sup>12</sup>

The absorption effect leads to the overheating of the metal vapor plume, which can be operated as an additional heat source. The absorbed energy can be dissipated by radiation and the convective heat transfer method. The equation of the secondary heat from the convection and radiation can be written as the following equation:

$$q_{\text{absorption}} = h_c(T_{\text{vap}} - T_{\text{key}}) - \sigma \varepsilon_r (T_{\text{vap}}^4 - T_{\text{key}}^4), \quad (15)$$

where  $h_c$  is the coefficient of the convective heat transfer,  $\sigma$  is the Stefan-Boltzmann constant,  $T_{\text{vap}}$  is the vapor temperature,  $T_{\text{key}}$  is the temperature on the keyhole wall, and  $\varepsilon_r$  is the emissivity. Here,  $T_{\text{vap}}$  is not input as an estimated value, which is determined by a numerical iteration method. Based on our previous work, the iteration method is used to guarantee that the total energy absorbed from scattering and the absorption effect is equal to the value calculated by Eqs. (11)–(13).

The momentum effect caused by the metal vapor plume on the keyhole wall is also considered according to the work from Cho *et al.*<sup>9</sup> The momentum effect from the impact of the high-velocity vapor can be divided into stagnation pressure and shear stress. The mathematical equation is shown in the following:

$$\tau_{\text{vapor}} = \frac{1}{8} f \rho_{\text{vapor}} (V \sin \theta)^2, \quad (16)$$

$$P_{\text{vapor}} = \frac{1}{2} \rho_{\text{vapor}} (V \cos \theta)^2, \quad (17)$$

where  $f = 64/Re$ ,  $\rho_{\text{vapor}}$  is the gas density,  $\theta$  is the angle between the normal vector of the free face and vertical direction,  $V$  is the vapor plume ejection velocity. The vapor ejection velocity is determined as 150 m/s on the keyhole outlet, which is assumed to increase linearly along the depth from 0 m/s at the keyhole bottom to the outlet. The vapor momentum effect is not considered in this model when the plume height is 0 mm.

### C. Numerical setup

The computational domain is defined with the dimensions of  $32 \times 12 \times 8 \text{ mm}^3$ . A fine hexahedral mesh region in the central part ( $-2.9 \leq y \leq 2.9 \text{ mm}$  and  $3 \leq x \leq 29 \text{ mm}$ ) is drawn, where the

10 November 2023 09:37:13

molten pool forms, with a recommended and fixed size of 0.2 mm, according to Ref. 23. The periphery of the finely meshed region is encompassed by coarser cells, whose size grows from an initial dimension of 0.2 mm and governed by a growth rate of 1.1. All transport equations are solved by the commercial software ANSYS FLUENT. The discretization of the momentum and energy conservation equations was executed utilizing a second-order upwind algorithm. The pressure implicit with splitting of operators is employed to calculate the velocity-pressure coupling. The aluminum-air interface is reconstructed by the Geo-Reconstruct method. The numerical simulations were conducted by a high-performance computing cluster at the Bundesanstalt für Materialforschung und prüfung (BAM) with 88 CPU cores and 1024 GB RAM. About 154 h computational time was consumed to simulate 0.75 s physical welding time.

#### IV. RESULTS AND DISCUSSION

The molten pool on the cross section is compared between experimental results, the reference case without considering the metal vapor plume effect, and the case with the metal vapor plume whose height is defined by a sine function. In Fig. 3, the black line is the profile of the final weld, and the red region represents the calculated weld region. The deviation of the molten pool width between the experimental results and the results without considering the vapor plume can be 22%. It can be clearly seen that there is a good agreement between the experimental weld profile and the calculation results when taking into account the oscillating metal vapor plume model. Since the metal vapor plume mainly affects the top surface, there is no apparent difference in keyhole depth between the case with/without the consideration of the metal vapor plume.

The oscillating metal vapor plume significantly influences the distribution of thermal energy on the top surface. Consequently, the temperature field is compared between the reference case without/with the metal vapor plume effect. The black profile line

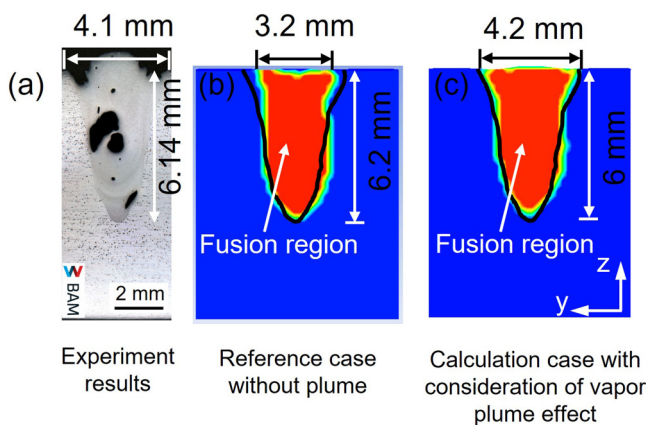


**FIG. 3.** Comparison between experimental and calculated fusion zones on cross section: (a) experiment results; (b) calculated results without vapor plume; (c) calculated results with consideration of the vapor plume effect.

represents liquidus temperature. As the metal vapor plume effect is included in the numerical model, a clear and significant increase in both the length and width of the weld pool can be observed in Fig. 4. This can be attributed to the scattering and absorption effect on the laser radiation by the metal vapor plume, leading to the redistribution of thermal energy on the top surface as an additional heat source. The molten pool length obtained by the case with metal vapor plume is closely approached with the experimental results (8.8 mm).

Considering the oscillatory nature of the integrated metal vapor plume in this model, described by a sine function, the temperature field is extracted and compared at two significant time points within one periodical cycle, as depicted in Figs. 4(b) and 4(c). In Fig. 4(b), the temperature field is extracted from time point A, which means the beginning point of a periodical cycle. Notably, the width of the high-temperature region (defined as the region with temperatures above 1250 K) in Fig. 4(b) is observed to be 21% smaller compared to that extracted from time point B in Fig. 4(c). At time point B, the high-temperature region is expanded due to the top surface exerting a whole additional heat flux from the metal vapor plume. Therefore, the molten pool is wider than

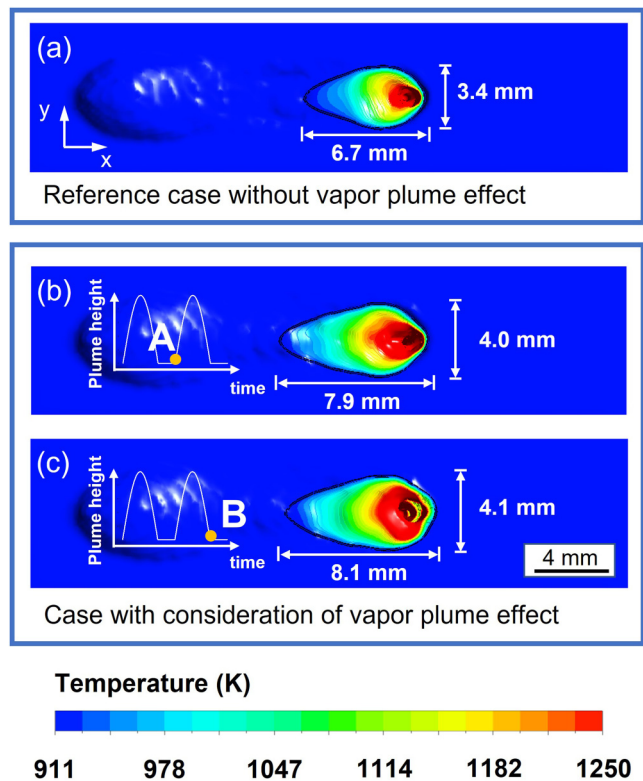


**FIG. 4.** Comparison of the temperature field between the reference case without/with the metal vapor plume effect: (a) the temperature field without the vapor plume effect; (b) the temperature field on the start point of one periodical cycle when the metal vapor plume effect is considered; (c) the temperature field on the endpoint of one sine wave.

10 November 2023 09:37:13

that at time point A. Compared with the vapor model without oscillation nature characteristic,<sup>9,12</sup> the width of the high-temperature region exhibits fluctuation because of the oscillating metal vapor plume. It should be noted that the expansion and shrinkage of the high-temperature region cannot be observed in some oscillating cycles. Due to the fluctuation in both the keyhole and molten pool, the absorbed laser energy is varied in nature. This variation, in turn, influences the fluctuation of the high-temperature region. It can be inferred that the fluctuation of the high-temperature region induced by the oscillating plume effect can be covered sometimes.

The laser beam energy absorbed on the keyhole wall is further influenced by the attenuation resulting from the scattering and absorption effect of the oscillating metal vapor plume. To investigate this, the absorption energy on the keyhole wall is extracted and compared between the reference case and the case considering the metal vapor plume effect, as shown in Fig. 5. The average laser beam energy absorbed on the keyhole wall is about 3380 W when the metal vapor plume effect is not integrated into the numerical model. As observed in Fig. 5(b), the laser beam energy absorbed on the keyhole wall oscillates with the height of the metal vapor plume. As the height of the metal vapor plume increases, more laser power is affected by the scattering and absorption effect, and the affected energy is mainly redistributed on the top surface of the metal plates through scattering, convective, and radiative mechanisms. The maximum total power attenuation can reach up to

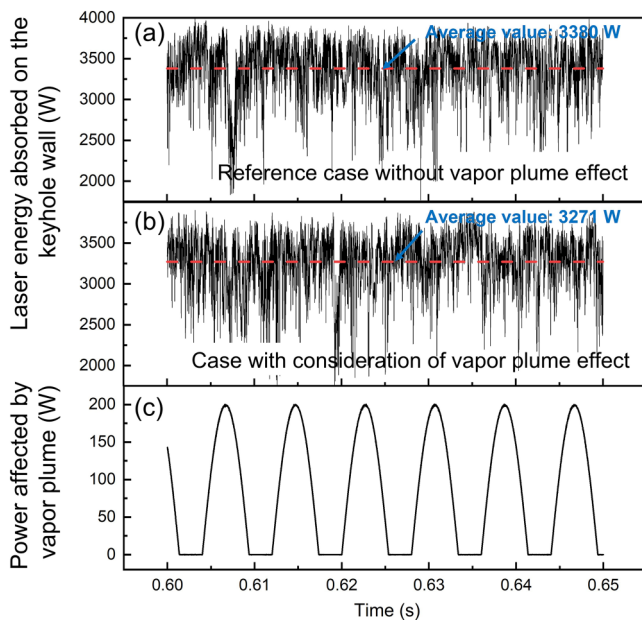


**FIG. 5.** The comparison of laser beam energy absorbed on the keyhole wall between the case with/without considering the metal vapor plume effect: (a) laser beam energy absorbed on the keyhole wall without the metal vapor plume effect; (b) laser beam energy absorbed on the keyhole wall with the metal vapor plume; (c) power affected by the scattering and absorption effect of the metal vapor plume.

200 W. As the height of the metal vapor plume is zero, it indicates there is no effect on the laser radiation, the laser can penetrate into the keyhole without any attenuation. Consequently, the laser beam energy absorbed on the keyhole wall is also affected by the metal vapor plume, which significantly affects the keyhole dynamics. Additionally, the average laser beam energy absorbed on the keyhole wall decreases to 3271 W when the metal vapor plume is considered in the model. Compared to our previous work, which treated the metal vapor plume model as a continuous process without considering the oscillating nature, this model avoids overestimating the laser beam energy on the keyhole wall.

The normalized time-averaged laser beam energy distribution absorbed on the keyhole wall (within 300 ms) is provided in Fig. 6. It can be seen from Fig. 6 that there is no noticeable difference in the laser beam energy distribution pattern on the keyhole wall between the calculation case with/without the consideration of the metal vapor plume. The laser beam energy absorbed on the keyhole wall mainly focuses on the top and bottom regions of the molten pool. When integrating the metal vapor plume into the calculation case, a slightly higher amount of laser beam energy is absorbed on the central region of the keyhole wall. Additionally,

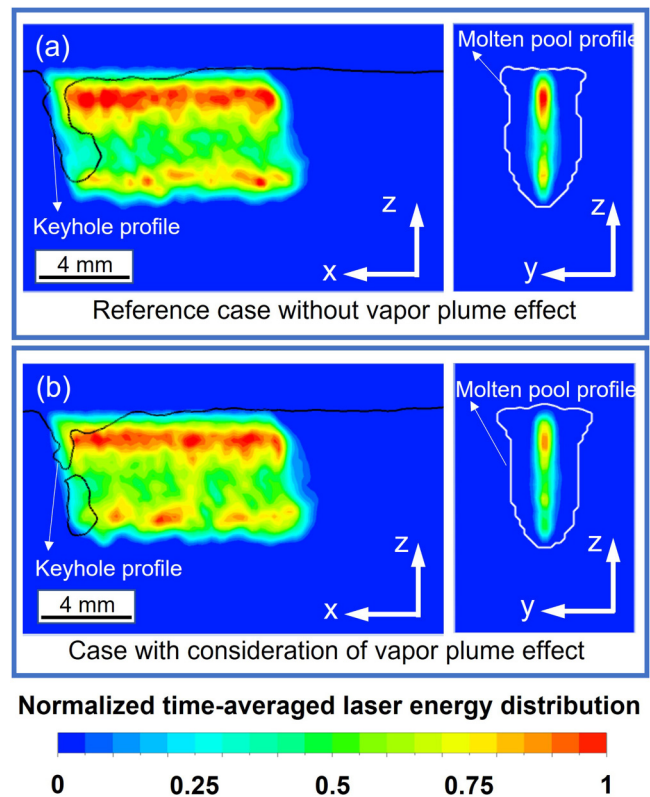


**FIG. 6.** Normalized time-averaged laser beam energy distribution absorbed on the keyhole wall: (a) reference case without metal vapor plume effect; (b) case with consideration of metal vapor plume effect.



compared to the reference case without the metal vapor plume, the case with the consideration of the metal vapor plume shows less laser beam energy absorbed on the top keyhole wall. It can be inferred that the secondary heating source applied on the top surface benefits the keyhole to keep it open. The laser ray is easier to escape from the keyhole. The direct laser beam energy distribution pattern on the keyhole wall has no apparent changes and less laser energy is absorbed on the top region. Therefore, the top profile of the molten pool shows a significant difference and can be clearly concluded by the scattering and absorption effect of the oscillating metal vapor plume.

The statistical comparison of keyhole collapse probability between the case without the metal vapor plume and the case with the metal vapor plume is conducted, as shown in Fig. 7. The

keyhole behavior exhibits pronounced differences between these two calculation cases. The keyhole collapse on the bottom is significant for the bubble formation, which is the main reason for the porosity generation.<sup>21</sup> Therefore, the keyhole collapse that happened within a distance of 1 mm relative to the keyhole bottom is counted. Based on Fig. 7(b), the keyhole collapse probability within a distance of 1 mm from the keyhole bottom reaches up to 75% as the metal vapor plume effect is integrated into the numerical model. However, the collapse probability within the same 1 mm distance is only 58% without considering the metal vapor plume effect. This increase primarily originates from the attenuated laser beam power with high-frequency oscillation, thereby causing the laser beam energy absorbed on the keyhole wall oscillation. The recoil pressure induced by evaporation is closely associated with laser beam energy precipitate on the keyhole wall. The force balance on the keyhole bottom can be broken more frequently due to the oscillating laser power. Consequently, considering the effect of the oscillating metal vapor plume on the laser beam attenuation in the numerical model increases the susceptibility of keyhole collapse. The increased susceptibility of the keyhole collapse on the bottom induced by the periodical oscillating laser power may correlate with the process porosity formation, but it still needs further study.

The occurrence of keyhole collapse at the top (within a distance of 2.4 to 4.6 mm relative to the keyhole bottom) is more frequent, with a probability of 8%, than the calculation case with the metal vapor plume. The collapse on the top region decreases to 5% when the metal vapor plume effect is integrated. This also confirms the above inference that the secondary heating source added on the top surface reduces the top keyhole collapse and keeps the keyhole open. The reason for the reduction of the top keyhole collapse probability is mainly due to the momentum exerted by the metal vapor plume. Based on the previously mentioned metal vapor plume model, a stagnation pressure is exerted on the keyhole wall. This stagnation pressure is directly proportional to the vapor ejection velocity that increased linearly, starting from zero at the bottom and reaching its maximum at the keyhole outlet. As a result, the stagnation pressure becomes larger in the top region compared to the bottom. The presence of this stagnation pressure, originating from the metal vapor plume, enhances the keyhole stability on the top region. Furthermore, the thermal energy introduced by the metal vapor plume on the top surface also plays an important role in keeping the keyhole open with less collapse.

10 November 2023 09:37:13

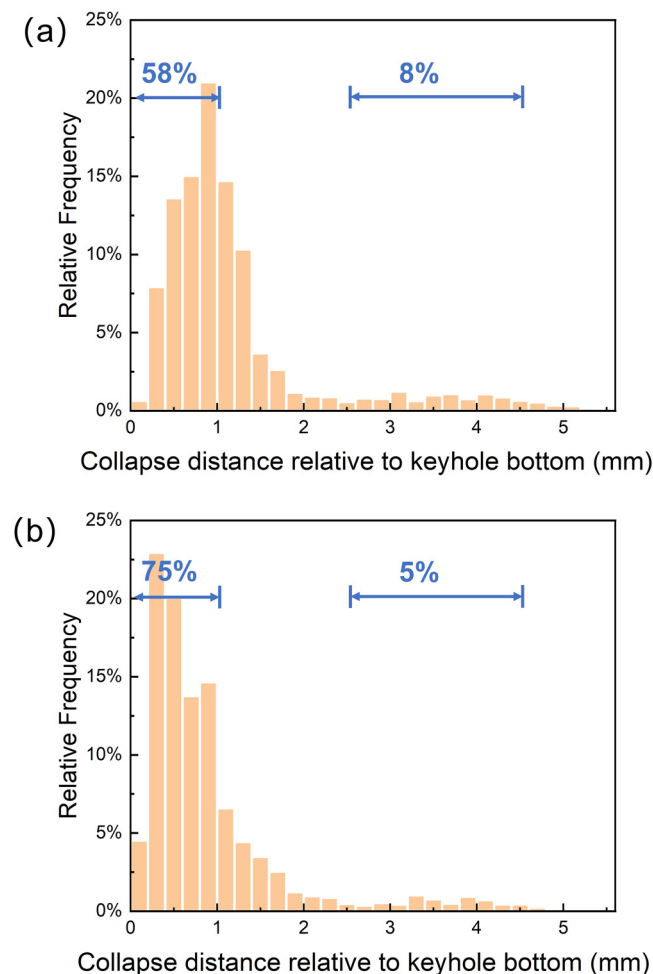


**FIG. 7.** Probability histogram of the keyhole collapse distance relative to keyhole bottom: (a) calculated results without considering metal vapor plume effect; (b) calculated results with considering metal vapor plume.

## V. CONCLUSIONS

1. A 3D transient heat transfer and fluid flow model coupled with the oscillating metal vapor plume is developed. The model has been validated by comparing numerically the obtained results to experimental measurements, which shows good agreement.
2. The metal vapor plume introduces an additional heat source on the top surface of the workpiece, which widens the top molten pool. In addition, the oscillating metal vapor plume caused fluctuations in the high-temperature region in the top molten pool.
3. The oscillating metal vapor plume increases the probability of keyhole collapse on the bottom from 58% to 75%. This can be attributed to the high-frequency oscillation of the attenuated

laser power, which increases the susceptibility of the keyhole instability on the keyhole bottom.

## ACKNOWLEDGMENTS

This work is funded by China Scholarship Council (No. 202008080270) and the Deutsche Forschungsgemeinschaft (DFG, German Research Foundation)—Project Nos. 506270597 and 466939224.

## AUTHOR DECLARATIONS

### Conflict of Interest

The authors have no conflicts to disclose.

### Author Contributions

**Fan Yang:** Data curation (equal); Formal analysis (equal); Investigation (equal); Methodology (equal); Software (equal); Validation (equal); Visualization (equal); Writing – original draft (equal). **Xiangmeng Meng:** Formal analysis (equal); Methodology (equal); Writing – review & editing (equal). **Stephen Nugraha Putra:** Methodology (equal). **Antoni Artinov:** Writing – review & editing (equal). **Marcel Bachmann:** Funding acquisition (equal); Project administration (equal); Resources (equal); Supervision (equal); Writing – review & editing (equal). **Michael Rethmeier:** Funding acquisition (equal); Project administration (equal); Resources (equal); Supervision (equal); Writing – review & editing (equal).

## REFERENCES

- <sup>1</sup>M. Bachmann, A. Gumenyuk, and M. Rethmeier, “Welding with high-power lasers: Trends and developments,” in *Proceedings of 9th International Conference on Laser Assisted Net Shape Engineering, Fürth, Germany, 19–22 September 2016* [Phys. Procedia **83**, 15–25 (2016)].
- <sup>2</sup>S. Katayama, *Handbook of Laser Welding Technologies* (Woodhead Publishing, Cambridge, UK, 2013), p. 108.
- <sup>3</sup>K. R. Kim and D. F. Farson, “CO<sub>2</sub> laser–plume interaction in materials processing,” *J. Appl. Phys.* **89**, 681–688 (2001).
- <sup>4</sup>J. Greses, P. A. Hilton, C. Y. Barlow, and W. M. Steen, “Laser–vapour interaction in high-power cw Nd:YAG laser welding,” in *International Congress on Applications of Lasers & Electro-Optics, Jacksonville, FL, USA, 13–16 October 2003* (Laser Institute of America, Orlando, FL, 2003), p. 546.
- <sup>5</sup>P. Y. Shcheglov, A. V. Gumenyuk, I. B. Gornushkin, M. Rethmeier, and V. N. Petrovskiy, “Vapor–plasma plume investigation during high-power fiber laser welding,” *Laser Phys.* **23**, 016001 (2013).
- <sup>6</sup>J. Zou, W. Yang, S. Wu, Y. He, and R. Xiao, “Effect of plume on weld penetration during high-power fiber laser welding,” *J. Laser Appl.* **28**, 022003 (2016).

- <sup>7</sup>J. Reijonen, A. Revuelta, T. Riipinen, K. Ruusuvoori, and P. Puukko, “On the effect of shielding gas flow on porosity and melt pool geometry in laser powder bed fusion additive manufacturing,” *Add. Manuf.* **32**, 101030 (2020).
- <sup>8</sup>S. Pang, X. Chen, W. Li, X. Shao, and S. Gong, “Efficient multiple time scale method for modeling compressible vapor plume dynamics inside transient keyhole during fiber laser welding,” *Opt. Laser Technol.* **77**, 203–214 (2016).
- <sup>9</sup>W. I. Cho, S. J. Na, C. Thomy, and F. Vollertsen, “Numerical simulation of molten pool dynamics in high power disk laser welding,” *J. Mater. Proc. Technol.* **212**, 262–275 (2012).
- <sup>10</sup>W. Tan, N. S. Bailey, and Y. C. Shin, “Investigation of keyhole plume and molten pool based on a three-dimensional dynamic model with sharp interface formulation,” *J. Phys. D: Appl. Phys.* **46**, 055501 (2013).
- <sup>11</sup>W. Tan and Y. C. Shin, “Analysis of multi-phase interaction and its effects on keyhole dynamics with a multi-physics numerical model,” *J. Phys. D: Appl. Phys.* **47**, 345501 (2014).
- <sup>12</sup>S. W. Han, W. I. Cho, L. J. Zhang, and S. J. Na, “A study on laser keyhole welding in vacuum by computational fluid dynamics simulations with plume effect models,” *J. Laser Appl.* **33**, 012042 (2021).
- <sup>13</sup>V. R. Voller and C. Prakash, “A fixed grid numerical modelling methodology for convection-diffusion mushy region phase-change problems,” *Int. J. Heat Mass Transfer* **30**, 1709–1719 (1987).
- <sup>14</sup>J. U. Brackbill, D. B. Kothe, and C. Zemach, “A continuum method for modeling surface tension,” *J. Comput. Phys.* **100**, 335–354 (1992).
- <sup>15</sup>A. Artinov, X. Meng, M. Bachmann, and M. Rethmeier, “Study on the transition behavior of the bulging effect during deep penetration laser beam welding,” *Int. J. Heat Mass Transfer* **184**, 122171 (2022).
- <sup>16</sup>C. W. Hirt and B. D. Nichols, “Volume of fluid (VOF) method for the dynamics of free boundaries,” *J. Comput. Phys.* **39**, 201–225 (1981).
- <sup>17</sup>Won-Ik Cho Suck-Joo Na, Claus Thomy, and Frank Vollertsen, “Numerical simulation of molten pool dynamics in high power disk laser welding,” *J. Mater. Proc. Technol.* **212**, 262–275 (2012).
- <sup>18</sup>X. Meng, A. Artinov, M. Bachmann, Ö Üstündağ, A. Gumenyuk, and M. Rethmeier, “The detrimental molten pool narrowing phenomenon in wire feed laser beam welding and its suppression by magnetohydrodynamic technique,” *Int. J. Heat Mass Transfer* **193**, 122913 (2022).
- <sup>19</sup>S. W. Han, J. Ahn, and S. J. Na, “A study on ray tracing method for CFD simulations of laser keyhole welding: Progressive search method,” *Welding World* **60**, 247–258 (2016).
- <sup>20</sup>S. Pang, X. Chen, J. Zhou, X. Shao, and C. Wang, “3D transient multiphase model for keyhole, vapor plume, and weld pool dynamics in laser welding including the ambient pressure effect,” *Opt. Lasers Eng.* **74**, 47–58 (2015).
- <sup>21</sup>R. Lin, H. P. Wang, F. Lu, J. Solomon, and B. E. Carlson, “Numerical study of keyhole dynamics and keyhole-induced porosity formation in remote laser welding of Al alloys,” *Int. J. Heat Mass Transfer* **108**, 244–256 (2017).
- <sup>22</sup>S. Muhammad, S. W. Han, S. J. Na, A. Gumenyuk, and M. Rethmeier, “Study on the role of recondensation flux in high power laser welding by computational fluid dynamics simulations,” *J. Laser Appl.* **30**, 012013 (2018).
- <sup>23</sup>W. I. Cho and S. J. Na, “Impact of wavelengths of CO<sub>2</sub>, disk, and green lasers on fusion zone shape in laser welding of steel,” *J. Welding Join.* **38**, 235–240 (2020).